NJC

Accepted Manuscript

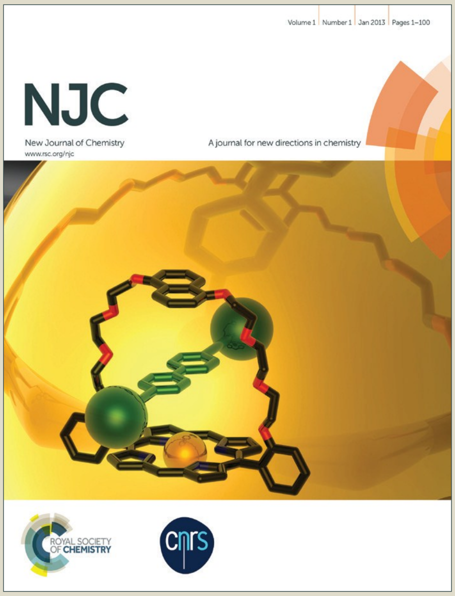

ROYAL SOCIETY OF CHEMISTRY

www.rsc.org/njc

Journal Name

RSCPublishing

ARTICLE

Cite this: DOI: 10.1039/x0xx00000x

Received 00th January 2012,
Accepted 00th January 2012

DOI: 10.1039/x0xx00000x

www.rsc.org/

TD-DFT and Structural Investigation of Natural Photosensitive Phenanthroperylene Quinone Derivatives

Ashley L. Shoaf[a] and Craig A. Bayse*[a]

Natural product derivatives of phenanthro[1,10,9,8-*opqra*]perylene-7,14-dione (PPD) are important potential agents in photodynamic therapy. Density functional theory (DFT) optimized geometries and time-dependent DFT (TD-DFT) vertical transitions of fringelite D (a pigment from an extinct species of sea lily), hypericin (an active component of Saint John's wort), stentorin C (*Stentor coeruleus*), blepharismin C (*Blepharisma japonicum*) and amethystin (*Stentor amethystinus*) are in good agreement with experimental structural, IR and UV-Vis data. The structure of the newly isolated amethystin has not been fully determined, but comparisons between the experimental and DFT IR frequencies suggest that this compound most likely adopts an orthoester structure. The π→π* excitations in the molecules are traceable to the PPD core, and are bathochromically shifted due to the peri –OH substituents with a smaller effect from the molecular twist induced by bay –Me and/or –OH groups. Hydrogen bonding between the peri –OH groups and the carbonyls are important to the ability of these species to photochemically general singlet oxygen and superoxide ions.

Introduction

Natural products based upon the phenanthro[1,10,9,8-*opqra*]perylene-7,14-dione (PPD, **1**) chromophore[1,2] are important photosensitizers with extended π-conjugated systems and have potential application in photodynamic therapy (PDT).[3] Colorful derivatives of **1** are found in various organisms including plants from the genus *Hypericum*[4] and the ciliates *Stentor*[5] and *Blepharisma*[6] (Figure 1). Fringelite D (**2**), a red pigment from an extinct species of sea lily,[7,8] may have functioned as an ingestion deterrent. Hypericin (**3**), isolated from *Hypericum perforatum* (St. John's wort), is also red and causes hypericism, a condition that triggers severe sensitivity to sunlight, intense skin irritation, elevated body temperatures and sometimes death.[1,3] **3** has been used in traditional medicine to treat depression,[9] but may be effective against viral and bacterial infections,[3,10–12] and cancer.[9,13] Hydrogen bonding interactions between **3** and the N7 position of guanine and adenine can disrupt DNA function[14,15] to inhibit the replication process of various viruses including FV (Friend leukemia virus), Rad-LV (radiation-induced leukemia virus), and EIAV (equine infectious anemia virus).[9–11,15] Stentorin C (**4**) is a blue pigment isolated from *Stentor coeruleus*[5] (Figure 1a) structurally determined by total synthesis as the 3,3'-diisopropyl derivative.[16] Blepharismin C (**5**) is the primary pigment produced by *Blepharisma japonicum* (Figure 1b).[6,17]

Amethystin (**6**) was recently isolated from *Stentor amethystinus* and is distinguishable from its stentorin and blepharismin relatives by its violet color (Figure 1c).[18] Three structures have been proposed for **6**: orthoester **A** (solution-phase), lactone isomer **B** (possible crystal form), and free acid **C** (suggested by elemental analysis but inconsistent with IR data). Amethystin (**6**) has been proposed to act as either a photosensor or for defense.[18] The biosynthetic pathway for **5** and **6** is proposed to be similar to that of **3** and **4** with the cycloheptatriene ring and phenol group originating from the addition *p*-hydroxyphenylglyoxylic acid to the protostentorin intermediate.[19–21]

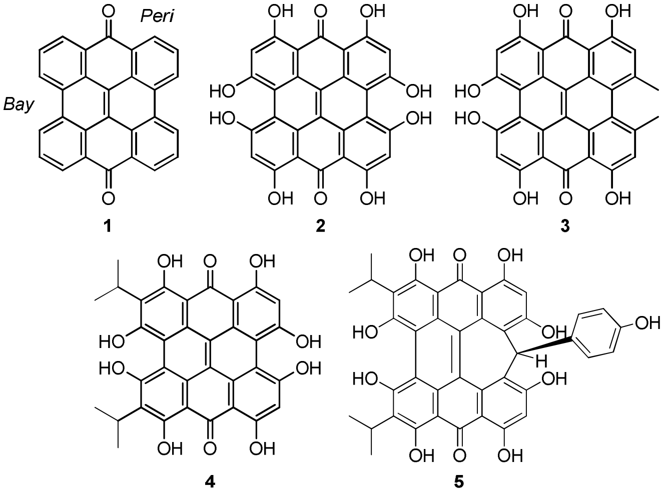

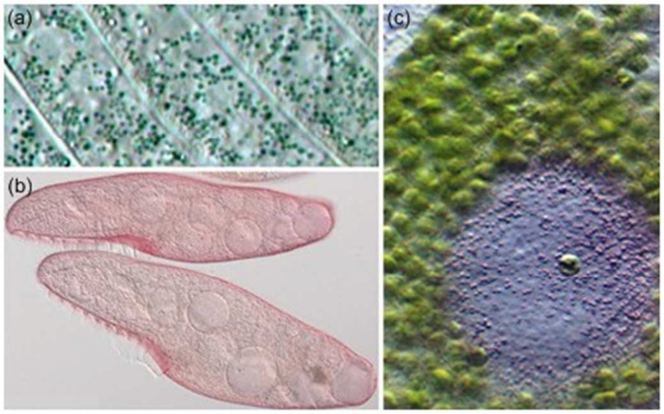

Figure 1. (a) Pigment-containing granules of *Stentor coeruleus* (b) *Blepharisma japonicum* organisms, and (c) *Stentor amethystinus* granules. (*S. coeruleus* and *S. amethystinus* provided with permission from Michael Plewka (plingfactory.de); *B. japonicum* provided with permission from Gerald Helbig (lebendkulturen.de).)

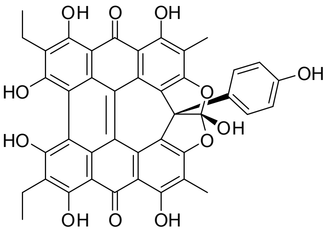

6A

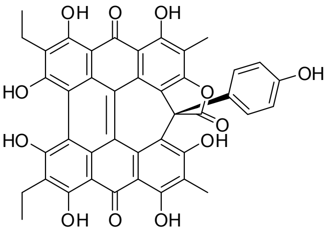

6B

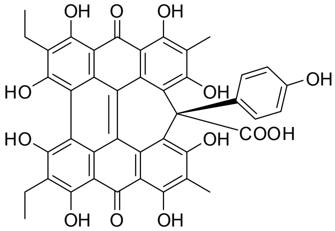

6C

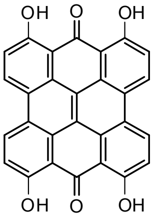

7

How the structural features of these colorful compounds affect their absorption spectra is important for understanding their mechanisms of photoactivity. Density functional theory (DFT) and time-dependent DFT (TD-DFT) methods, shown to be useful for the prediction of properties of PDT agents,[22–25] have been used to examine the structures and electronic transitions in the UV-Vis region of **2-6** for comparison to experimental data and the parent PPD (**1**) and to suggest the structure for **6**. These results show that the photoexcitations of these natural products can be traced to the structural modifications of the parent PPD chromophore.

Theoretical Methods

1-6 were optimized with Gaussian 09[26] using DFT and a series of exchange correlation (xc) functionals (M06-L,[27] mPW1PW91,[28] B3LYP, PBE0, ωB97, BLYP, TPSSh, LC-ωPBE, CAM-B3LYP). Geometries were optimized with the split-valence triple-ζ plus polarization functions (TZVP). Calculations in larger basis sets (cc-pVTZ, TZVP+, TZV2P+, TZV2P+f) provided similar optimized structures and theoretical excitation spectra. Uncorrected vibrational frequencies were calculated to verify the structures as minima on the potential energy surface. The modelling of the excitation spectra of PPD derivatives is consistent with established procedures for the calculation of vertical transitions in dye molecules.[29–31] TD-DFT was used to produce the first 30 singlet vertical excitations for comparison to experimental UV-Vis spectra. This approach typically leads to inaccuracies of 0.24-0.41 eV based upon a comparison of vertical and 0-0 transitions for a series of large molecules.[32] Although optimized geometries were similar in all functionals, TD-DFT vertical excitations calculated with the hybrid functionals B3LYP, mPW1PW91, PBE0 and ωB97 were found to underestimate and the pure functional BLYP to overestimate the experimental excitation wavelengths of **1** (Table S1†). The ωB97 transition wavelengths were particularly poor (underestimated by ~100 nm). The PBE0 and B3LYP xc functionals are commonly used and typically predict vertical transitions to within 0.2 eV. However, the TPSSh and M06-L functionals gave the best agreement with the experimental values for the compounds under examination in this work. The M06-L was found to be more accurate for the calculation of vertical TD-DFT transitions than other pure functionals.[33] In select cases, the vibrationally-corrected excitation spectrum was calculated from the TD-DFT-optimized geometry of the first singlet excited state using the Franck-Condon-Herzberg-Teller method as implemented by the FCClasses routines.[34–36] Geometry optimizations and vertical TD-DFT calculations were performed in the gas-phase and using the integral equation formalism variant of the polarisable continuum mode (IEF-PCM) implicit solvation method[37] with solvents that correspond to the experiment (DMSO (**1**), THF (**2**), ethanol (**3** and **5**), and methanol (**4** and **6**)). PCM-type solvation models are most applicable when modelling systems in which there is no hydrogen bonding. As a result, the inclusion of implicit solvation effects often does not significantly affect the transition energies.[33]

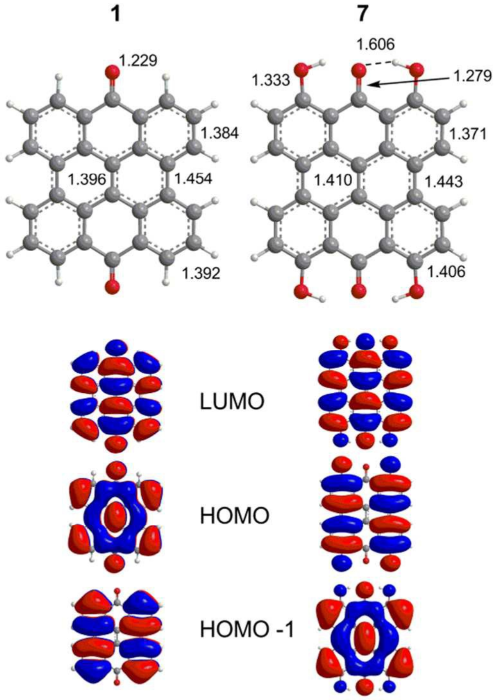

Figure 2. DFT(TPSSh)/TZVP optimized geometries of **1** and **7** with MOs relevant to the excitation spectrum as determined by TD-DFT calculations.

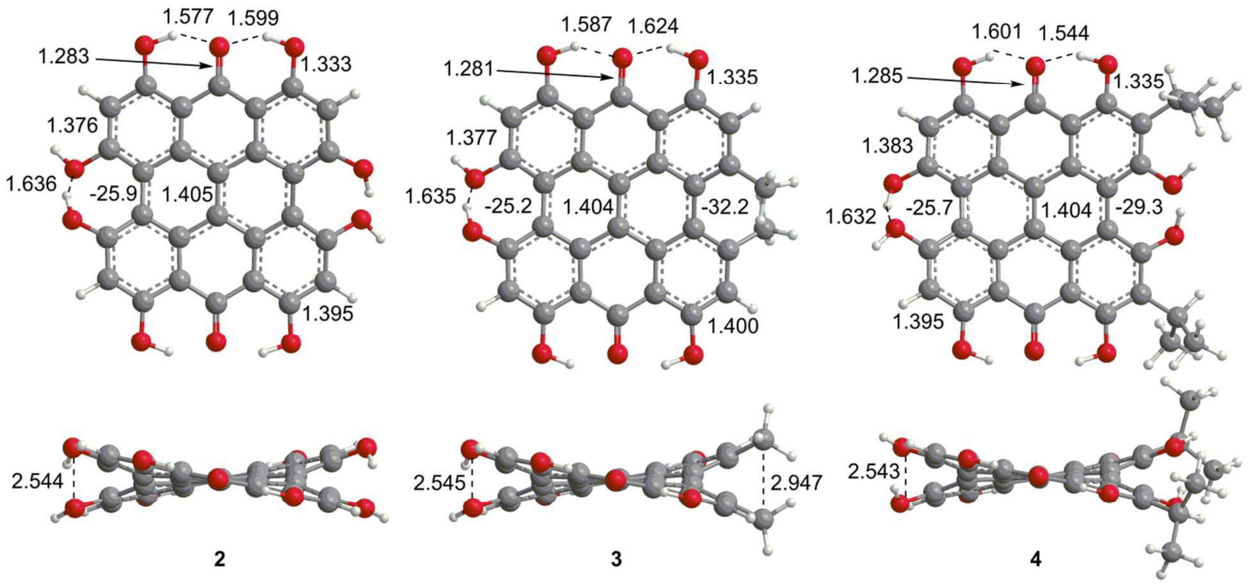

Figure 3. DFT(TPSSh/TZVP) optimized geometries for the propeller conformation of **2-4** in gas phase. Bond distances are listed in Å..

Results and Discussion

Phenanthro[1,10,9,8-opqra]perylene-7,14-dione (PPD, 1). The extended π-conjugated system of **1** is the structural backbone for the colorful and potentially therapeutic natural products **2-6**. **1** is generally insoluble in common organic solvents and its fluorescence is observed in protic, but not aprotic solvents.[38] Two bands are observed experimentally in the visible region (423 and 410 nm). The DFT(TPSSh)/TZVP optimized geometry of **1** (D_{2h}, Figure 2) displayed a strong carbonyl stretch at 1725 cm^{-1} comparable to the experimental value (1661 cm^{-1} KBr).[39] TD-DFT calculations find two vertical transitions with significant oscillator strengths (*f*, a measure of the predicted intensity) in the visible region (gas-phase: 437 nm, 433 nm; DMSO: 459 nm, 456 nm) in agreement with previous Pariser-Parr-Pople calculations.[40] These two bands are roughly consistent with the 423 nm experimental peak and are assigned as $\pi \rightarrow \pi^*$ type transitions (HOMO-1→LUMO and HOMO→LUMO, respectively, Figure 2).

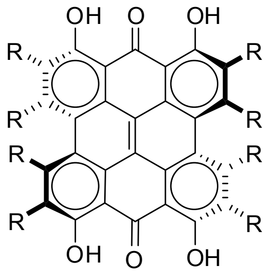

propeller

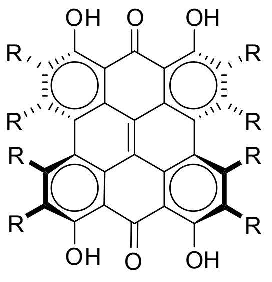

double-butterfly

Fringelite D (2), Hypericin (3) and Stentorin C (4). Steric interactions between the bay –OH and/or –Me groups force compounds **2-4** into nonplanar conformations, principally the "propeller" and the "double-butterfly" conformations.[1,7,41,42] The propeller is the most stable for **2-4** with the double-butterfly being slightly higher in energy (DFT(M06-L)/TZVP, ΔE = 2.4 kcal/mol, 2.7 kcal/mol, 2.8 kcal/mol, respectively), consistent with the X-ray[43] and molecular mechanics structure of **3**.[44] Only the major tautomers[44,45] were considered with the maximum hydrogen bonding between –OH and carbonyl groups. Both peri –OH groups are hydrogen bonded to the carbonyls and one hydrogen bond is assumed between the bay –OH groups. The minimum conformation of **2** and **4** orients the hydrogen bonds of the two sets of bay –OH groups in opposite directions (Fig 3). The hydrogen bonds with the peri –OH groups weaken the carbonyl bond and extend the aromaticity of the system by forming cyclic interactions that satisfy the Hückel rule. Breaking any one of the hydrogen bonding interactions leads to a higher energy structure (~30.0 kcal/mol if all interactions are broken). Enantiomers of the propeller and double-butterfly conformations were identical in energy. Interconversion between the propeller, double-butterfly and their enantiomers may occur at room temperature due to the low barrier for twisting the bay hydroxyl groups (6.7 kcal/mol).[44] However, only one conformer of **3** is observed in NMR studies.[46] DFT(TPSSh)/TZVP bond distances and dihedrals for **3** compare favorably to previous DFT studies,[47] and structural parameters for **2** and **4** were very similar to **3**. The gas-phase vibrational frequencies for **2-4** correlate well to reported experimental IR values.[5,7,48] An abridged list of the major frequencies can be found in Table 1.

Wavelengths, oscillator strengths (*f*), and MOs for the TD-DFT(TPSSh) vertical transitions of **2-4** are generally in good agreement with the experimental spectra and early Pariser-Parr-Pople calculations (Table 2).[40,41,49,50] Calculations on the propeller and double-butterfly conformations gave similar excitation wavelengths in the gas phase and the PCM solvation model, thus only the propeller will be described in the following discussion. Experimentally, 5-6 absorption bands are observed in the 330–600 nm range for **2-4** and assigned as $\pi \rightarrow \pi^*$ excitations. Based on the TD-DFT transitions (Table 2), the three bands can be assigned to major electronic transitions in analogy to the interpretation of the UV-Vis spectrum of **3**.[49] The $S_0 \rightarrow S_1$ excitation is found at 570–600 nm and assigned as the HOMO→LUMO excitation, bathochromically shifted relative to **1**. The natural transition orbitals[51] for these excitations are similar in character to the HOMO and LUMO and are shown in the Supplementary Materials (Figure S1). The $S_0 \rightarrow S_2$ band at 475-480 nm are generally lower in intensity and assigned as having HOMO-1→LUMO and/or HOMO-2→LUMO character. For **3**, the experimental band at 385 nm is attributed to the HOMO→LUMO+1 excitation, but is very low intensity (f=0.02) and not reported for **2** and **4.** A more intense band observed in the region 330–340 nm corresponds to the HOMO→LUMO+2 excitation mixed with contributions from other transitions. Other bands in the UV-Vis spectrum are attributed to vibronic coupling to the electronic transitions (*vide infra*).

Table 1. Comparison of experimental (in italics) and selected DFT(TPSSh)/TZVP vibrational frequencies for the propeller conformation of **2-4**.

mode	**2**	**3**	**4**
O-H, bay	3505, 3770	3511, 3771	3481, 3513, 3737, 3774
C-H str, ring (w)	3174 (w)	3174, 3180	3174
C-H str, chain (w)		3042, 3091, 3095, 3139, 3142	3006-3031, 3070-3096, 3106, 3114, 3122, 3132
O-H, peri	2977, 3095	3003, 3045, 3106, 3128	2888, 2965, 3037, 3105
C=O	1670 *1572*[a]	1663, 1667 *1620*[b]	1664 *1600*[c]
ring	1305, 1316, 1335, 1375, 1414, 1472, 1438, 1493, 1513, 1566, 1603, 1618, 1640 *1437*[a], *1419*[a], *1272*[a]	1298, 1334, 1363-1373, 1411, 1426, 1472, 1501-1525, 1605, 1623, 1626, 1636 *1560*[b]	1296, 1310, 1333, 1371, 1400, 1415, 1437, 1459, 1473, 1495, 1511, 1523, 1599, 1610-1618, 1640 *1587*[c]
C-H, O-H wag	1183, 1209, 1225 *1175*[a], *1110*[a]	1178, 1210, 1225, 1273 *1064*[b]	1202-1215, 1240

a. Reference 7, b. Reference [48], c. Reference 5

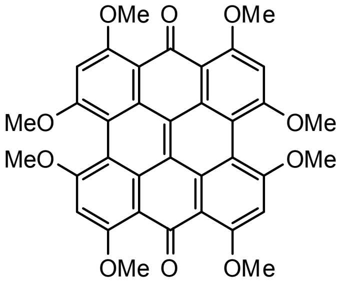

8

The characters of the MOs of **2-4**, particularly for the most symmetric **2** (point group: C_2), are clearly traceable to their analogues in **1** (compare Figure 2 and 4). The peri hydroxyls are the major contributor to the destabilization of the MOs relative to **1** with minor contribution from the twist. Calculations of the PPD core substituted only at the peri position (**7**, fringelite H, Figure 2) show that the antibonding character between the parent π system and the p-type orbitals of the peri –OH groups shifts the HOMO–LUMO excitation to 575 nm and destabilizes the MO analogous to HOMO-1 in **1** to the HOMO as shown for **2-4**. The hydrogen bonding interactions between the peri –OH groups and the carbonyls are also important to the electronic structure of **2-4**. The per-methylated derivative **8** has a similar C=O bond length and HOMO to **1**, but its HOMO-1 and HOMO-2 are lone pair MOs of the carbonyls. These results suggest that aromatization in the peri region is necessary to destabilize the π system through further delocalization. A similar effect may occur when protonation of **1** and per-methylated **3** shifts their photophysical properties to be more similar to **3**.[45] The molecular twist further shifts the HOMO–LUMO transition by 10-20 nm (Table 2) and leads to the additional excitation bands versus **1** observed in the experimental spectra. In **3**, the replacement of one set of bay –OH groups with –Me groups enhances the twist on one side of the molecule due to increased repulsion (Figure 3). The *i*-Pr groups in **4** also decrease the symmetry, but to a lesser extent, leading to minor distortions in the π lobes relative to **2**. HOMO-1, analogous to the HOMO of **1**, is destabilized by the twisting of the PPD backbone which partially disrupts the donut-like lobe (Figure 4). The enhanced twist and asymmetry of **3** and **4** further destabilize HOMO-1 to shift the transition of these electrons to longer wavelengths (Table 2).

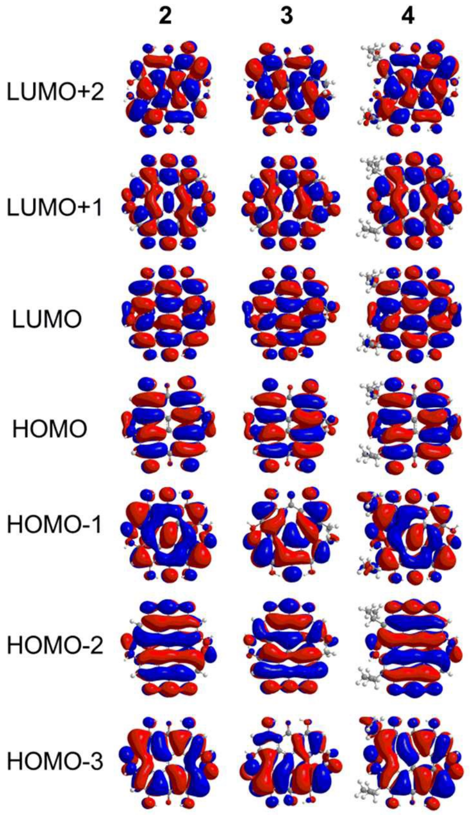

Figure 4. MOs contributing to the UV-Vis excitations for **2-4** as calculated with TD-DFT.

The experimental spectra of **2-4** contain peaks in the 500–555 nm range that do not correlate with the vertical TD-DFT transitions. In a detailed analysis of **3**, Wynn and Cotton assign this band as absorption to a vibronic level of the $S_0 \rightarrow S_1$ excitation. The vibrationally corrected spectrum of **2** was calculated from the TD-DFT(PBE0)/TZVP-optimized structure of the first excited state (Figure 5) using the Franck-Condon-Herzberg-Teller method. The 0-0 transition was predicted at 564 nm with vibronically coupled bands at 550, 523 and 488 nm. These bands can be attributed to the 545, 1402 and 1530 cm^{-1} modes of the excited state, all of which include stretching or wagging motions of the peri –OH groups. Like related

Table 2. Assignment of experimental UV-Vis bands to selected vertical TD-DFT (TPSSh/TZVP) transitions for the propeller conformation of **2-4**.

	Exp[a] (λ/nm)	Vertical excitation wavelength, nm (oscillation strength)				Excitations (TPSSh)
		TPSSh/TZVP	M06-L/TZVP	IEF-PCM-M06-L/TZVP	PBE0/TZVP	
2	577	572 (0.21)	583 (0.20)	591 (0.30)	522 (0.26) 564[c], 550[c]	0.70 HOMO→LUMO
	536[b] 501[b]				523[c] 488[c]	
	443	457 (0.16)	471 (0.15)	466 (0.29)	414 (0.21)	0.68 HOMO-2 → LUMO – 0.16 HOMO-3 → LUMO
	419	391 (0.02)	403 (0.02)	413 (0.02)	357 (0.02)	0.68 HOMO-4 → LUMO – 0.16 HOMO → LUMO+2
	334	337 (0.27)	345 (0.23)	344 (0.37)	310 (0.40)	0.63 HOMO → LUMO+2 + 0.13 HOMO → LUMO+4 + 0.14 HOMO-1 → LUMO – 0.11 HOMO-2 → LUMO+1 – 0.10 HOMO-4 → LUMO
3	591	587 (0.22)	599 (0.21)	602 (0.30)	533 (0.26)	0.69 HOMO → LUMO
	547[b] 510[b]					
	475	475 (0.10)	493 (0.06)	485 (0.20)	427 (0.18)	0.64 HOMO-1 → LUMO + 0.22 HOMO-2 → LUMO + 0.14 HOMO-3 → LUMO
		456 (0.07)	474 (0.09)	475 (0.07)	412 (0.04)	0.66 HOMO-2 → LUMO – 0.19 HOMO-1 → LUMO
	382	416 (0.04)	396 (0.01)	390 (0.01)	369 (0.02)	0.55 HOMO → LUMO+1 + 0.10 HOMO-1 → LUMO – 0.36 HOMO-3 → LUMO + 0.21 HOMO-4 → LUMO
	332	334 (0.15)	341 (0.10)	337 (0.28)	306 (0.27)	0.59 HOMO → LUMO+2 – 0.12 HOMO → LUMO+3 + 0.21 HOMO → LUMO+4 + 0.22 HOMO-2 → LUMO+1 – 0.10 HOMO-8 → LUMO
4	598	574 (0.24)	584 (0.23)	591 (0.31)	523 (0.28)	0.70 HOMO → LUMO
	554[b] 516[b]					
	452	477 (0.17)	491 (0.16)	486 (0.27)	432 (0.23)	0.67 HOMO-1 → LUMO + 0.13 HOMO → LUMO+2 + 0.13 HOMO-3 → LUMO
	344	338 (0.22)	346 (0.32)	342 (0.32)	310 (0.37)	0.60 HOMO → LUMO+2 + 0.11 HOMO → LUMO+3 + 0.11 HOMO → LUMO+4 – 0.12 HOMO-1 → LUMO – 0.10 HOMO-4 → LUMO + 0.17 HOMO-8 → LUMO + 0.14 HOMO-9 → LUMO

[a] Experimental in THF for **2**,[7] EtOH for **3**,[49] and MeOH for **4**.[53] IEF-PCM calculations were performed in MeOH.

[b] Experimenal bands attributed to vibronic coupling.

[c] Vibronically coupled excitations calculated using the Franck-Condon-Herzberg-Teller method.

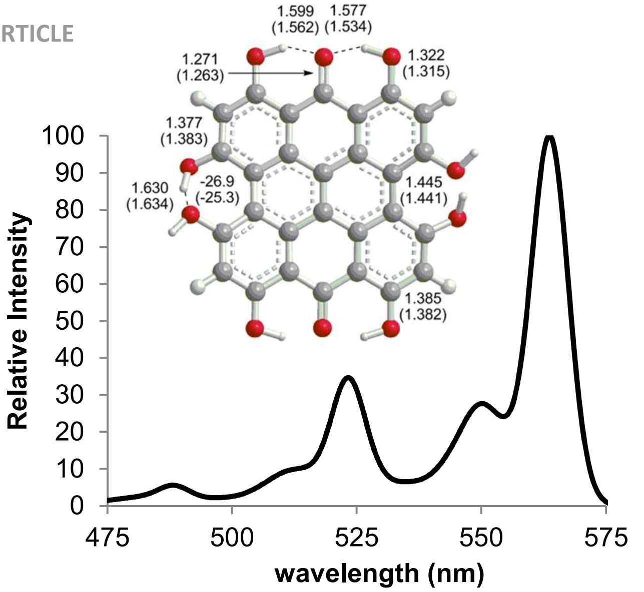

Figure 5. Selected bond distances for the ground state (DFT(PBE0)/TZVP) and first excited state (TD-DFT(PBE0)/TZVP) of **2** and the vibronically coupled UV-Vis spectrum of **2** at 300K calculated using the Franck-Condon-Herzberg-Teller method.

studies of anthraquinone derivatives,[52] the shape of the predicted spectrum (Figure 5) is in very good agreement with the reported experimental spectrum (Table 2), with the 550 nm band assigned as a shoulder commonly observed on the main absorption of these PPD derivatives. Vibronic bands in the spectra of **3**-**6** are assigned on the basis of structural similarities of the PPD derivatives leading to coupling of the excitations with vibrational modes involving the peri OH groups.

Blepharismin C (5) and Amethystin (6). Like **2**-**4**, blepharismin C (**5**) and amethystin (**6**) are based upon the PPD core, but modified during biosynthesis to incorporate a phenyl ring attached to a cycloheptatriene fragment (Figure 6). Steric interactions between the bay region –OH groups can force **5** into a "saddle" conformation[54] with the twist occurring on the end opposite of the cycloheptatriene ring, in addition to the propeller and the double-butterfly conformations.[6,17] For **5**, the saddle conformation is the most stable at the DFT(TPSSh)/TZVP level (Figure 6). All attempts at optimization of the propeller and double-butterfly resulted in the saddle because the cycloheptatriene ring prevents the correct twist for the propeller and double-butterfly conformations. The *endo*-isomer (Figure 5) with the phenol above the saddle was more stable than the *exo*-isomer by 5.6 kcal/mol in good agreement with experimental NMR data.[55,56] Previous semi-empirical (AM1) studies showed that the *endo*-isomer is more stable than the *exo*-isomer (Figure 6) and the interconversion barrier is high (43 kcal/mol) due to the steric interactions required to invert the ring and pass the phenyl group through the bay hydroxyl groups.[54,56] Another semi-empirical (PM3) study suggested that the *exo*-isomer in the propeller conformation was most stable but the structure did not include intramolecular hydrogen bonding interactions of the bay and peri –OH groups.[6] The DFT vibrational frequency and intensity of the asymmetric carbonyl stretching mode (1617 cm^{-1}) is consistent with the strong peak at 1597 cm^{-1} in the experimental IR spectrum.[17]

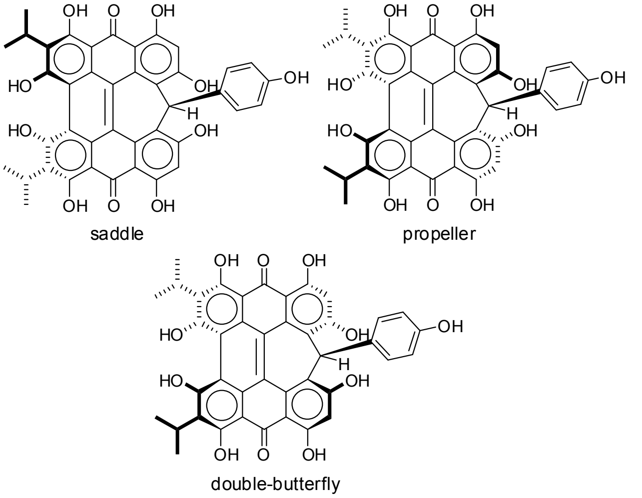

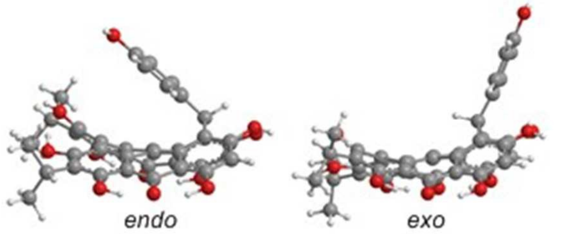

Figure 6. DFT(M06-L)/TZVP optimized structures of **5** for the *endo*- and *exo*-isomers in the saddle conformation in gas phase, with the *endo*-isomer being most stable.

Table 3. Selected DFT(TPSSh)/TZVP vibrational frequencies of **5** and **6A**.

mode	5	6A
O-H, bay	3403, 3623-3693, 3786	3539, 3733-3878
C-H str, arom (w)	3172-3215	3152-3198
C-H str, chain (w)	3028-3037, 3087-3128	2968, 3030-3060, 3089, 3099-3137
O-H, peri	2936-2962, 3063, 3167	2911, 3029, 3083, 3095
ring, complex	1214, 1240, 1293, 1319, 1343, 1359, 1371-1382, 1417, 1445, 1465, 1487, 1504-1512, 1595-1601, 1615-1620, 1634, 1661, 1666	1140-1173, 1200, 1290-1300, 1320-1347, 1360, 1374, 1437, 1472, 1485, 1503, 1544, 1574, 1611, 1618, 1632, 1641-1644,
ring Ph	1542	1187
C-H, O-H wag	1190	

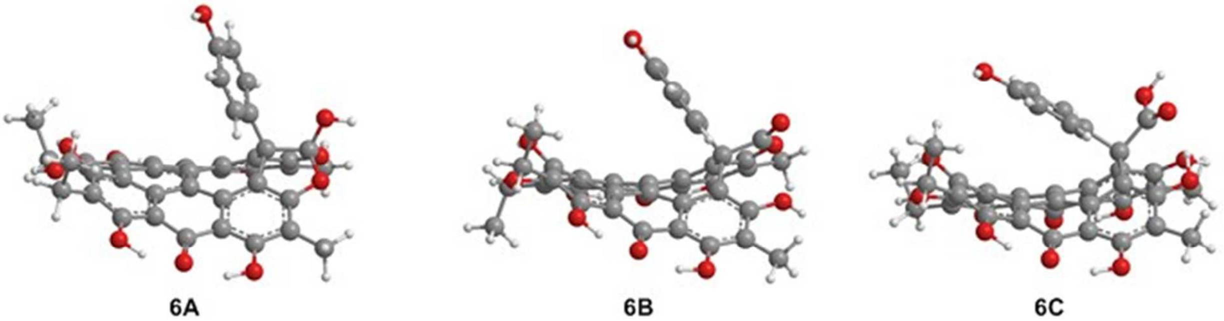

Figure 7. DFT(TPSSh)/TZVP optimized geometries of possible structures of **6** in the gas phase. The orthoester **6A** is the preferred structure based upon IR analysis.

Table 4. Assignment of experimental UV-Vis bands to selected vertical TD-DFT(TPSSh)/TZVP transitions for **5** and **6A**.

	Exp[a] (λ/nm)	Vertical excitation wavelength, nm (oscillation strength)				Excitations (TPSSh)
		TPSSh/TZVP	M06-L/TZVP	IEF-PCM-M06-L/TZVP[c]	PBE0/TZVP	
5	~580	568 (0.19)	583 (0.17)	0.17 (0.24)	512 (0.23)	0.69 HOMO → LUMO
	~540[b]					
	~490	490 (0.14)	503 (0.13)	0.13 (0.22)	448 (0.10)	0.52 HOMO-2 → LUMO – 0.46 HOMO-1 → LUMO
	~340	345 (0.11)	355 (0.08)	0.08 (0.09)	313 (0.18)	0.61 HOMO → LUMO+2 – 0.12 HOMO-6 → LUMO – 0.18 HOMO-9 → LUMO – 0.11 HOMO-11 → LUMO
6A Saddle	579	568 (0.19)	583 (0.18)	585 (0.26)	510 (0.24)	0.70 HOMO → LUMO
	538[b]					
	494	500 (0.08)	524 (0.04)	523 (0.08)	448 (0.21)	0.52 HOMO-1 → LUMO – 0.46 HOMO-2 → LUMO
		488 (0.09)	505 (0.15)	507 (0.20)		0.53 HOMO-2 → LUMO – 0.46 HOMO-1 → LUMO
	355	323 (0.10)	347 (0.04)	349 (0.04)	332 (0.08)	0.40 HOMO → LUMO+3 + 0.12 HOMO-1 → LUMO+2 + 0.31 HOMO-3 → LUMO+3 + 0.16 HOMO-4 → LUMO+3 + 0.12 HOMO-6 → LUMO+3 + 0.30 HOMO-10 → LUMO+2 – 0.13 HOMO-11 → LUMO+2

[a] Experimental in EtOH for **5** and in MeOH for **6A**. IEF-PCM calculations were performed in MeOH.
[b] Experimenal bands attributed to vibronic coupling.

The three structures proposed for **6** (the orthoester **A**, the lactone isomer **B**, and the free acid **C**) may adopt nonplanar conformations similar to **5** (Figure 7).[18] For **6A**, the saddle conformation is the most stable with all attempts of optimization in propeller and double-butterfly resulting in the saddle. However, both saddle and propeller conformations were found for **6B** and **6C** because these structures are not restricted by the orthoester rings of **6A**. The propeller is most stable for **6B** (2.8 kcal/mol), and **6C** has the saddle as the lowest energy conformation (20.7 kcal/mol). DFT vibrational frequencies for **6A-C** were compared to experimental data in order to assign the most probable structure. The DFT frequencies of **6A** (Table 3) are most consistent with the available IR data and the experimental assignment based on the presence of only quinone carbonyl peaks and a weak carbonyl band at 1798 cm^{-1}. The lack of an active mode in **6A** around 1798 cm^{-1} suggests that experimental IR spectrum may contain a mixture, most likely of **6C** for which the DFT C=O stretching frequency was found at 1785 cm^{-1}.

Wavelengths and oscillator strengths (*f*) for the TD-DFT transitions for **5** and **6A** were similar in the gas phase and in solvent and consistent with the experimental spectra. **6A** was the best match with the experimental wavelengths (Table 4 and Table S2†). In the range 340–580 nm, four peaks are observed experimentally for **5** and **6A** (Table 4) which are assigned to $\pi\rightarrow\pi^*$ transitions based on the TD-DFT calculated spectra. The $S_0\rightarrow S_1$ band around 580 nm corresponds to the HOMO→LUMO excitation (Figure 8) which is bathochromically shifted relative to **1** due to the destabilization of the HOMO by peri –OH groups as discussed for **2-4**. Despite the structural changes to these molecules, the frontier MOs of **5** and **6A** have similar character and vertical TD-DFT(TPSSh) transitions to **2-4** (compare Figures 2, 4, and 8). The quaternary carbon and orthoester rings stabilize the conformation of **6A** and cause minor changes in the MOs when compared to **5**. No vertical TD-DFT transition is found corresponding to the ~540 nm band which is assigned as a vibronic level based upon analogy to **2**. The experimental excitation in the 490–495 nm range is assigned to the HOMO-2→LUMO and HOMO-1→LUMO excitations but the TD-DFT wavelengths are roughly 10 nm longer than the experimental values. The band between 340–360 nm corresponds to a mixture of higher energy excitations in **5** and **6A**. HOMO-2 and HOMO-1 have large contributions from the phenol group of **5** in these excitations suggesting a charge-transfer component to the photoactivity which may be modified through substitutions to the phenol ring. These MOs bear less resemblance to the MOs due to the contributions of the phenol ring and the disruption of the extended π system by the cycloheptatriene ring. LUMO+2 of **5** has a minor contribution from the phenol group, but **6A** has no contribution from the phenol group.

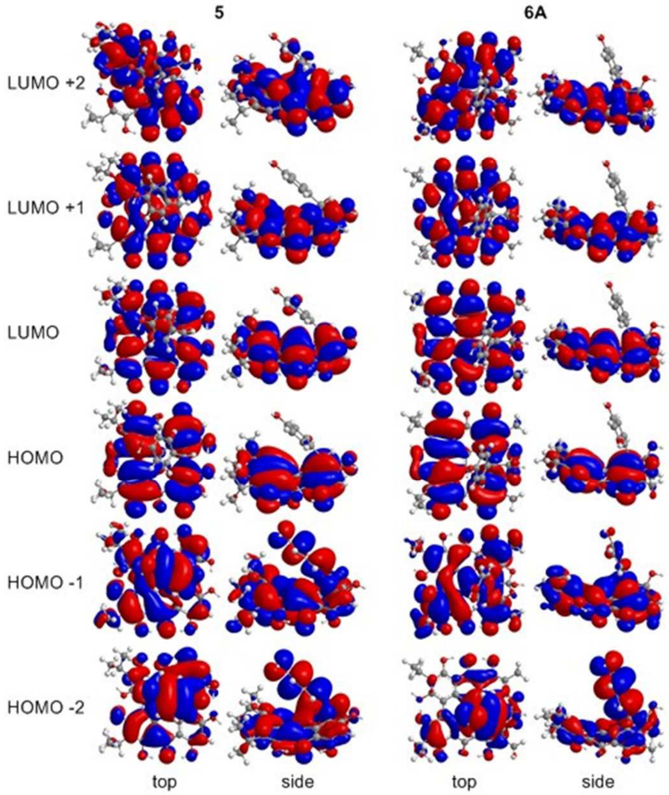

Figure 8. MOs contributing to the UV-Vis excitations for **5** and **6A** as calculated with TD-DFT.

Type I and II Photochemical Reactions. In an oxygen environment, the excited state triplet of photosensitizers (PS) either react initially with target molecules to form radical anions which are then scavenged by oxygen (Type I) or the triplet state of the PS can be quenched by $^3O_2$ to form singlet oxygen (Type II).

$$\text{Type I:}\quad PS(T_1) + S \rightarrow PS^{-\cdot} + S^{+\cdot}$$
$$PS^{-\cdot} + {}^3O_2 \rightarrow PS(S_0) + O_2^{-\cdot}$$
$$\text{Type II:}\quad PS(T_1) + {}^3O_2 \rightarrow PS(S_0) + {}^1O_2$$

In Type I mechanisms, a potential PS is effective if electron transfer to oxygen to form superoxide ions is thermodynamically favourable. Type II mechanisms are favourable if the singlet-triplet gap ($\Delta E_{S\text{-}T}$) for the PS is greater than for oxygen. These criteria can be estimated from the vertical electron affinities (VEA), adiabatic electron affinities (AEA) and $\Delta E_{S\text{-}T}$ values (Table 5). For the type I mechanism, the larger VEA for the triplet state relative to the ground state indicates the general ability of the excited PPD derivatives to oxidize surrounding molecules.[47] Comparison of the AEAs of the PS radical anion and $^3O_2$ suggest reduction to superoxide is favourable by 0.05-0.1 eV for the AEA of triplet oxygen calculated at the same level of theory. The VEA and AEA values for **3** are comparable to a previous study by Guedes and Eriksson[47] in which a more favourable energy difference (0.4 eV) was predicted based upon an $^3O_2$ AEA of 3.91 eV. For the Type II mechanism, each of the PPD derivatives have a higher $\Delta E_{S\text{-}T}$ than the $^3\Sigma_g^- \rightarrow {}^1\Delta_g$ transition of oxygen (0.98 eV) and would be predicted to catalyze the production of singlet oxygen. In contrast, although the singlet-triplet gap (1.80 eV) of **8** is similar to **2-6**, its VEA are too low to sustain Type I or Type II photochemical reactions, suggesting that the peri –OH-carbonyl hydrogen bonds are critical to photoactivity.

Table 5. DFT(M06-L)/TZVP vertical singlet-triplet gaps and electron affinities (eV) for PPD derivatives **2-6**.[a]

	solvent	$\Delta E_{S\text{-}T}$	VEA(S_0)	VEA(T_1)	AEA(S_0)
2	gas phase	1.59	1.88	3.48	2.01
	water	1.61	3.15	4.76	3.25
	DMSO	1.61	3.14	4.74	3.24
	MeOH	1.61	3.12	4.73	3.23
3	gas phase	1.56	1.92	3.47	2.03
	water	1.57	3.19	4.76	3.25
	DMSO	1.57	3.17	4.75	3.27
	MeOH	1.57	3.16	4.73	3.25
4	gas phase	1.60	1.82	3.42	1.94
	water	1.60	3.10	4.71	3.20
	DMSO	1.60	3.09	4.69	3.19
	MeOH	1.60	3.08	4.68	3.17
5	gas phase	1.66	1.80	3.46	1.94
	water	1.66	3.05	4.71	3.18
	DMSO	1.66	3.03	4.69	3.16
	MeOH	1.66	3.02	4.68	3.14
6	gas phase	1.65	1.76	3.42	1.91
	water	1.66	3.06	4.71	3.18
	DMSO	1.66	3.04	4.70	3.16
	MeOH	1.66	3.03	4.68	3.15

a. AEA for $^3O_2$: 3.36 (water), 3.33 (DMSO), 3.29 (MeOH) eV

Conclusions

Understanding the structure and photochemistry of these natural photosensitizers are important for determining why plants and ciliates use these compounds as well as how they can be modified to improve their medical application as photodynamic therapy agents. Phenanthro[1,10,9,8-opqra]perylene-7,14-dione (**1**) and its natural product derivatives (**2-7**) have been explored by calculating the optimized structure and UV-Vis spectrum using DFT and TD-DFT. The propeller conformation is most stable for **2-4**, and the saddle conformation is most stable for **5** and **6A**. For **6**, which is newly isolated and has not been fully characterized experimentally, DFT IR frequencies suggest that the orthoester **6A** is the most probable structure. The TD-DFT calculations of the vertical transition wavelengths and intensities are consistent with experimental spectra and assigned as π→π* excitations within the phenanthro[1,10,9,8-opqra]perylene-7,14-dione core of **2-6**. Peaks missing from the vertical TD-DFT spectra have been attributed to vibronic coupling to vibrational modes involving the peri –OH groups. The similarities in the bathochromic shift in λ_{max} observed in **2-6** and the additional features in the spectra compared to **1** are attributed to the peri –OH substitutions as in **7** and, to a lesser extent, the molecular twist induced by the bay –Me and/or –OH groups. The molecular orbitals of **2-7** are traceable to the shared chromophore, even for **5** and **6A**, which have the larger cycloheptatriene ring. Some excitations of **5** and **6A** involve orbital character on the phenol substituent suggesting a potential intramolecular charge transfer process that may be modified by substitution. Photochemical generation of superoxide and singlet oxygen is thermodynamically favourable for each of the natural product derivatives.

Acknowledgements

Calculations were performed using high performance clusters managed by ODU Information Technology Services. We thank Michael Plewka (www.plingfactory.de) for providing microscopic images of *Stentor coeruleus* and *Stentor amethystinus* and Gerald Helbig (www.lebendkulturen.de) for providing a microscopic image of *Blepharisma japonicum*. The authors thanks an anonymous reviewer for valuable comments on

Notes and references

The authors declare no competing financial interest.

[a] Deparment of Chemistry and Biochemistry, Old Dominion University, Norfolk, Virginia, 23529, United States.

*cbayse@odu.edu

† Electronic Supplementary Information (ESI) available: [Comparison of functionals and basis sets for **1**, experimental UV-Vis bands to TD-DFT transitions (M06-L/TZVP) for **6B** and **6C**, and Cartesian coordinates of **1-7** are presented]. See DOI: 10.1039/b000000x/

1. H. Falk, *Angew. Chem.-Int. Ed.*, 1999, **38**, 3117–3136.
2. C. A. Mulrooey, E. M. O'Brien, B. J. Morgan, and M. C. Kozlowski, *Eur. J. Org. Chem.*, 2012, 3887–3904.
3. N. Duráan and P.-S. Song, *Photochem. Photobiol.*, 1986, **43**, 677–680.
4. C. S. Lobban, S. J. Hallam, P. Mukherjee, and J. W. Petrich, *Photochem. Photobiol.*, 2007, **83**, 1074–1094.
5. N. Tao, M. Orlando, J. S. Hyon, M. Gross, and P. S. Song, *J. Am. Chem. Soc.*, 1993, **115**, 2526–2528.
6. M. Maeda, H. Naoki, T. Matsuoka, Y. Kato, H. Kotsuki, K. Utsumi, and T. Tanaka, *Tetrahedron Lett.*, 1997, **38**, 7411–7414.
7. H. Falk and E. Mayr, *Monatshefte Für Chem.*, 1995, **126**, 699–710.
8. H. Falk and E. Mayr, *Monatshefte Für Chem.*, 1997, **128**, 353–360.
9. G. A. Kraus, W. Zhang, S. Carpenter, and Y. Wannemuehler, *Bioorg. Med. Chem. Lett.*, 1995, **5**, 2633–2636.
10. D. Meruelo, G. Lavie, and D. Lavie, *Proc. Natl. Acad. Sci.*, 1988, **85**, 5230–5234.
11. G. Lavie, F. Valentine, B. Levin, Y. Mazur, G. Gallo, D. Lavie, D. Weiner, and D. Meruelo, *Proc. Natl. Acad. Sci.*, 1989, **86**, 5963–5967.
12. N. Kashef, Y. S. Borghei, and G. E. Djavid, *Photodiagnosis Photodyn. Ther.*, 2013, **10**, 150–155.
13. N. J. Wills, J. Park, J. Wen, S. Kesavan, G. A. Kraus, J. W. Petrich, and S. Carpenter, *Photochem. Photobiol.*, 2001, **74**, 216–220.
14. S. Sánchez-Cortés, P. Miskovsky, D. Jancura, and A. Bertoluzza, *J. Phys. Chem.*, 1996, **100**, 1938–1944.
15. P. Miskovsky, *Curr. Drug Targets*, 2002, **3**, 55–84.
16. D. W. Cameron and A. G. Riches, *Tetrahedron Lett.*, 1995, **36**, 2331–2334.
17. G. Checcucci, R. S. Shoemaker, E. Bini, R. Cerny, N. Tao, J.-S. Hyon, D. Gioffre, F. Ghetti, F. Lenci, and P.-S. Song, *J. Am. Chem. Soc.*, 1997, **119**, 5762–5763.
18. G. Höfle, S. Reinecke, U. Laude, and D. Spitzner, *J. Nat. Prod.*, 2014, **77**, 1383–1389.
19. G. Rodewald, R. Arnold, J. Griesler, and W. Steglich, *Angew. Chem. Int. Ed. Engl.*, 1977, **16**, 46–47.
20. H. Banks, D. Cameron, and W. Raverty, *Aust. J. Chem.*, 1976, **29**, 1509–1521.
21. H. P. Bais, R. Vepachedu, C. B. Lawrence, F. R. Stermitz, and J. M. Vivanco, *J. Biol. Chem.*, 2003, **278**, 32413–32422.
22. M. E. Alberto, C. Iuga, A. D. Quartarolo, and N. Russo, *J. Chem. Inf. Model.*, 2013, **53**, 2334–2340.
23. M. E. Alberto, T. Marino, A. D. Quartarolo, and N. Russo, *Phys. Chem. Chem. Phys.*, 2013, **15**, 16167–16171.
24. M. E. Alberto, B. C. De Simone, G. Mazzone, A. D. Quartarolo, and N. Russo, *J. Chem. Theory Comput.*, 2014, **10**, 4006–4013.
25. M. E. Alberto, G. Mazzone, A. D. Quartarolo, F. F. R. Sousa, E. Sicilia, and N. Russo, *J. Comput. Chem.*, 2014, **35**, 2107–2113.
26. *Gaussian 09*, Gaussian, Inc., Wallingford, CT, 2009.
27. Y. Zhao and D. G. Truhlar, *J. Chem. Phys.*, 2006, **125**, 194101.
28. C. Adamo and V. Barone, *J. Chem. Phys.*, 1998, **108**, 664–675.
29. D. Jacquemin, E. A. Perpète, I. Ciofini, and C. Adamo, *Acc. Chem. Res.*, 2009, **42**, 326–334.
30. A. D. Laurent and D. Jacquemin, *Int. J. Quantum Chem.*, 2013, **113**, 2019–2039.
31. A. D. Laurent, C. Adamo, and D. Jacquemin, *Phys. Chem. Chem. Phys.*, 2014, **16**, 14334–14356.
32. L. Goerigk, J. Moellmann, and S. Grimme, *Phys. Chem. Chem. Phys.*, 2009, **11**, 4611–4620.
33. D. Jacquemin, E. A. Perpète, I. Ciofini, C. Adamo, R. Valero, Y. Zhao, and D. G. Truhlar, *J. Chem. Theory Comput.*, 2010, **6**, 2071–2085.
34. F. Santoro, R. Improta, A. Lami, J. Bloino, and V. Barone, *J. Chem. Phys.*, 2007, **126**, 084509.
35. F. Santoro, A. Lami, R. Improta, and V. Barone, *J. Chem. Phys.*, 2007, **126**, 184102.
36. F. Santoro, A. Lami, R. Improta, J. Bloino, and V. Barone, *J. Chem. Phys.*, 2008, **128**, 224311.
37. J. Tomasi, B. Mennucci, and R. Cammi, *Chem. Rev.*, 2005, **105**, 2999–3094.
38. H. Falk and A. Vaisburg, *Monatshefte Für Chem.*, 1995, **126**, 361–364.
39. P. M. Donovan and L. T. Scott, *Polycycl. Aromat. Compd.*, 2008, **28**, 128–135.
40. C. Etzlstorfer, H. Falk, N. Muller, and T. N. H. Tran, *Monatshefte Für Chem.*, 1996, **127**, 659–668.
41. R. Altmann, C. Etzlstorfer, and H. Falk, *Monatshefte Für Chem.*, 1997, **128**, 785–793.
42. O. Pieroni, P. Plaza, M. Mahet, N. Angelini, G. Checcucci, M. Malatesta, M. M. Martin, and F. Lenci, *Photochem. Photobiol.*, 2005, **81**, 1343–1346.
43. D. Freeman, F. Frolow, E. Kapinus, D. Lavie, G. Lavie, D. Meruelo, and Y. Mazur, *J. Chem. Soc. Chem. Commun.*, 1994, 891–892.
44. C. Etzlstorfer, H. Falk, N. Muller, W. Schmitzberger, and U. Wagner, *Monatshefte Für Chem.*, 1993, **124**, 751–761.
45. F. Gai, M. J. Fehr, and J. W. Petrich, *J. Phys. Chem.*, 1994, **98**, 5784–5795.
46. A. Smirnov, D. B. Fulton, A. Andreotti, and J. W. Petrich, *J. Am. Chem. Soc.*, 1999, **121**, 7979–7988.
47. R. C. Guedes and L. A. Eriksson, *J. Photochem. Photobiol. - Chem.*, 2005, **172**, 293–299.
48. E. I. Kapinus, H. Falk, and H. T. N. Tran, *Monatshefte Für Chem.*, 1999, **130**, 623–635.

49. J. L. Wynn and T. M. Cotton, *J. Phys. Chem.*, 1995, **99**, 4317–4323.
50. T. Yamazaki, N. Ohta, I. Yamazaki, and P. S. Song, *J. Phys. Chem.*, 1993, **97**, 7870–7875.
51. R. L. Martin, *J. Chem. Phys.*, 2003, **118**, 4775–4777.
52. D. Jacquemin, E. Brémond, A. Planchat, I. Ciofini, and C. Adamo, *J. Chem. Theory Comput.*, 2011, **7**, 1882–1892.
53. H. Falk and E. Mayr, *Monatshefte Für Chem.*, 1995, **126**, 1311–1321.
54. T. G. Dax, C. Etzlstorfer, and H. Falk, *Monatshefte Für Chem.*, 2000, **131**, 1115–1122.
55. Y. Uruma, K. Sakamoto, K. Takumi, M. Doe, Y. Usuki, and H. Iio, *Tetrahedron*, 2007, **63**, 5548–5553.
56. D. Spitzner, G. Höfle, I. Klein, S. Pohlan, D. Ammermann, and L. Jaenicke, *Tetrahedron Lett.*, 1998, **39**, 4003–4006.

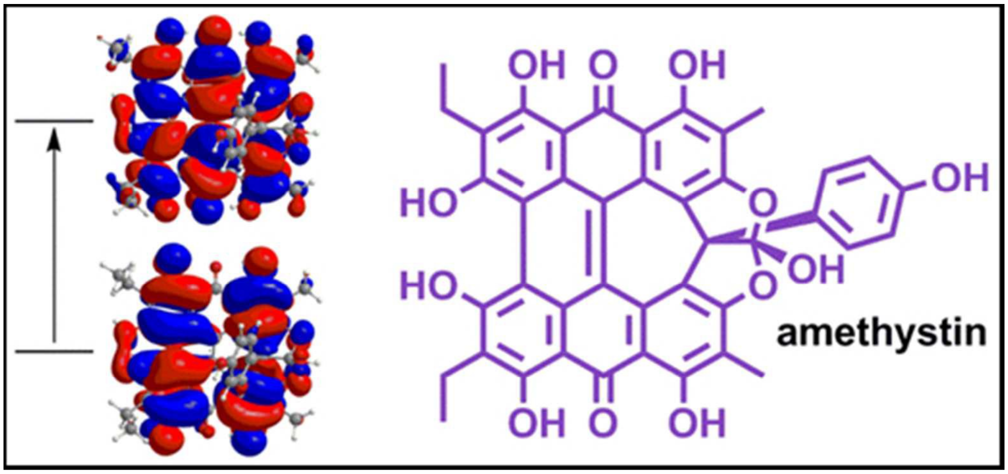

Structural modification of the phenanthroperylene quinone core affects the electronic structure of a series of natural product photosensitizers.